Supporting Information

Tailoring acidic microenvironments for carbon-efficient CO₂ electrolysis over Ni-N-C catalyst in a membrane electrode assembly electrolyzer

Hefei Li,‡[ab] Haobo Li,‡[a] Pengfei Wei,[ab] Yi Wang,[ab] Yipeng Zang,[a] Dunfeng Gao,*[a] Guoxiong Wang*[a] and Xinhe Bao*[a]

[a] State Key Laboratory of Catalysis, Dalian National Laboratory for Clean Energy, iChEM (Collaborative Innovation Center of Chemistry for Energy Materials), Dalian Institute of Chemical Physics, Chinese Academy of Sciences, Dalian 116023, China.
[b] University of Chinese Academy of Sciences, Beijing, 100049, China

‡ These authors contributed equally to this work

Corresponding authors. Email: dfgao@dicp.ac.cn; wanggx@dicp.ac.cn; xhbao@dicp.ac.cn

Experimental section

Chemicals and materials

Zinc nitrate hexahydrate ($Zn(NO_3)_2 \cdot 6H_2O$, AR), nickel nitrate hexahydrate ($Ni(NO_3)_2 \cdot 6H_2O$, AR), methanol (MeOH), potassium sulphate (K_2SO_4) and sulfuric acid (H_2SO_4) were purchased from Sinopharm Chemical Reagent Co., Ltd (China). 2-Methyl imidazole (2-MeIM, 98%) and potassium hydroxide (KOH) was purchased from Aladdin. Cobalt(II) phthalocyanine (CoPc) was purchased from Alfa Aesar. Ag nanoparticles were purchased from Macklin. Polytetrafluoroethylene (PTFE, 60 wt% dispersion in H_2O) were purchased from Sigma-Aldrich. Nafion HP membrane was purchased from DuPont™. Ir black was purchased from Johnson Matthey Corp. Ultrapure water (18.2 MΩ) was used in all experiments. All the chemicals were used without further purification.

Synthesis of catalysts

Ni-N-C catalyst was synthesized using a modified protocol according to our previously reported method.[1] 10 mM $Zn(NO_3)_2 \cdot 6H_2O$ and 20 mM $Ni(NO_3)_2 \cdot 6H_2O$ was first dispersed in 400 mL MeOH at 400 rpm. Then 300 mM 2-MeIM (dissolved in 100 mL MeOH) was added and kept continuous stirring for 24 h. After that, the violet precipitates (ZnNi ZIF-8 precursor) were collected by filtration and washed with MeOH and finally dried in vacuum. Finally, as-prepared ZnNi ZIF-8 precursor was heated to 1000 °C at a rate of 3 °C min^{-1} and kept at 1000 °C for 4 h in flowing Ar atmosphere, followed by cooling down to room temperature naturally. The as-obtained black

products were denoted as Ni-N-C catalyst. The Ni content was determined to be 4.0 wt.% by inductively coupled plasma optical emission spectroscopy (ICP-OES).

Preparation of gas diffusion layer (GDL)

Firstly, Vulcan XC-72R carbon black was dispersed in ethanol, and then PTFE was added with mechanically stirring to form a homogeneous ink. The ink was hand-painted onto one side of carbon paper (Toray TPG-H-60) and then was annealed in air at 350 °C for 1 h in a muffle furnace to obtain the final GDL.

Electrode preparation

Ni-N-C electrode: Ni-N-C catalyst and Nafion ionomer were dispersed in ethanol with a mass ratio of 9:1. Then the ink was painted onto the GDL to prepare the gas diffusion electrode (GDE). The mass loading of the catalyst was 1.5 mg cm^{-2}.

CoPc electrode: CoPc, XC-72R carbon black and Nafion ionomer were dispersed in ethanol with a mass ratio of 1.8:7.2:1. Then the ink was painted onto the GDL to prepare the GDE. The mass loading of CoPc was 0.3 mg cm^{-2}.

Ag nanoparticle electrode: Ag nanoparticles, XC-72R carbon black and Nafion ionomer were dispersed in ethanol with a mass ratio of 1.8:7.2:1. Then the ink was painted onto the GDL to prepare the GDE. The mass loading of Ag nanoparticles was 0.3 mg cm^{-2}.

Anode: Commercial Ir black catalyst and quaternary ammonia poly(N-methyl-piperidine-co-p-terphenyl) (QAPPT) ionomer solution were dispersed in ethanol with a mass ratio of 9:1. Then the ink was painted on a Ti foam to prepare the anode catalyst layer. The mass loading of Ir black was 1.0 mg cm^{-2}.

Material characterization

The powder X-ray diffraction (XRD) patterns of the catalysts were recorded with a PANalytical X'pert PPR diffractometer with a Cu $K\alpha$ radiation source (λ=1.5418 Å) at 40 kV and 40 mA at a scan rate of 5° min^{-1}. High-angle annular dark field-scanning transmission electron microscopy (HAADF-STEM) measurements were performed with JEM-ARM200F (JEOL, Japan, for high-resolution images). X-ray photoelectron spectroscopy (XPS) was recorded on a Thermo Scientific ESCALAB 250Xi spectrometer with an Al $K\alpha$ X-ray source. All the binding energies were calibrated with C 1s spectrum with peak intensity at 284.8 eV. The X-ray absorption fine structure (XAFS) spectra of Ni K edge was measured in fluorescence mode using a Lytle detector at the BL11B beamline at Shanghai Synchrotron Radiation Facility (SSRF). The energy was calibrated to the absorption edge of a Ni foil (8333 eV). The data was processed using the software package including Athena and Artemis.

CO_2 electrolysis measurements

CO_2 electrolysis experiments were performed in an acidic or alkaline membrane electrode assembly (MEA) electrolyzer (4 cm^2) as described previously.[2] The electrolyzer was assembled using a graphite and a Pt-coated titanium flow field plate for CO_2 feeding at the cathode, aqueous solution feeding at the anode, as well as for current collecting. The cathodic flow field was fed with dry 95% CO_2/5% N_2 at a total flow rate of 31 or 15.5 mL min^{-1} (thus, the flow rate of CO_2 was 29.5 or 14.7 mL min^{-1}). The anodic flow field was fed with a 1 M KOH or 0.5 M K_2SO_4 solution (with different pH values) continuously at a flow rate of 5 mL min^{-1} using a peristaltic pump. In details,

H_2SO_4 was used to adjust the pH of K_2SO_4 solution through a pH Meter (Shanghai leici, pHS-3C). And the total K^+ concentrations of all electrolytes were kept constant at 1 M. The anode and cathode compartments were separated by a QAPPT anion exchange membrane or a cation exchange membrane (Nafion HP with a thickness of 20 µm). The electrolysis was carried out in the galvanostatic mode using an Autolab potentiostat/galvanostat (PGSTAT 302 N with 10 A booster). In order to determine cell resistance, potentiostatic electrochemical impedance spectroscopy (EIS) was conducted at open circuit voltage (OCV) before electrocatalytic performance test. The potential amplitude was 10 mV and the frequency range was 0.1 Hz to 100 kHz. Two-step CO_2 electrolysis setup consists of an acidic MEA electrolyzer (25 cm^2) and an alkaline MEA electrolyzer (4 cm^2). The acidic electrolysis in the 25 cm^2 electrolyzer was carried out in the galvanostatic mode using an Ivium potentiostat/galvanostat (V83833 with 100 A booster). The cathodic 95% CO_2/5% N_2 flow rate was 180 mL min^{-1}. The anodic flow field was fed with 0.5 M K_2SO_4 + H_2SO_4 solution (pH 0.5) continuously at a flow rate of 30 mL min^{-1}. The currents applied to acidic MEA electrolyzer were 2.5, 5, 7.5, 10 and 12.5 A, respectively, and the current applied to alkaline MEA electrolyzer was fixed at 4 A. The outlet of the acidic MEA electrolyzer was connected to a CO_2 capture solution and a cold trap and then the alkaline MEA electrolyzer (4 cm^2).

Product analysis

Gas products in cathode and anode were analyzed by an on-line gas chromatography (GC, Agilent, GC490) equipped with thermal conductivity detector (TCD). H_2, O_2, N_2, CO can be detected in Channel 1 (with a Molsieve 5A column) of GC while Ar, CO_2

can be detected in Channel 2 (with a PoraPlot U column). In cathode outlet, gas products were directly flowing into the on-line GC. In anode outlet, a liquid gas mixture was firstly obtained and then separated in a flask. Argon was used as the carrier gas purging gas products to GC. Liquid products were analyzed by a Bruker AVANCE III 400 MHz nuclear magnetic resonance (NMR) spectrometer. A mixture of liquid electrolyte and 1-propanesulfonic acid 3-(trimethylsilyl) sodium salt (DSS, as an internal standard) was used for ^{1}H-NMR measurements. The one dimensional ^{1}H spectrum was measured with water suppression using a pre-saturation method. No liquid product was detected by ^{1}H-NMR. The error bars represent standard deviation from three independent measurements conducted under the same conditions.

The Faradaic efficiency of a specific product is calculated as follows:

$$\varepsilon_{Faradaic,i} = Q_i/Q_{total} \times 100 = (N_i \times n_i \times F)/Q_{total} \times 100$$

Where,

$\varepsilon_{Faradaic,i}$: the Faradaic efficiency of product i, %;

Q_{total}: the consumed charge, C;

Q_i: the charge used for the formation of the product i, C;

N_i: the amount of the product i, mol;

n_i: the number of electrons transferred to form the product i;

F: Faraday constant, which is 96485 C mol^{-1}.

Partial current density of a specific product is calculated as follows:

$$j_{partial,i} = j_{total} \times \varepsilon_{Faradaic,i}$$

The energy efficiency for the formation of a specific product is defined as follows:

$$\varepsilon_{Energy,i} = \frac{\Delta H_i^0}{\Delta G_i} \times \varepsilon_{Faradaic,i} = \frac{n_i \times F \times E^n}{n_i \times F \times E_i} \times \varepsilon_{Faradaic,i} = \frac{E^n}{E_i} \times \varepsilon_{Faradaic,i}$$

Where,

$\varepsilon_{Energy,i}$: the energy efficiency for the formation of product i, %;

ΔH_i^0: the theoretical enthalpy change of product i, kJ mol^{-1};

ΔG_i: the changes in the Gibbs free energy of product i, kJ mol^{-1};

$\varepsilon_{Faradaic,i}$: the Faradaic efficiency of product i, %;

n_i: the number of electrons transferred to form the product i;

F: Faraday constant, which is 96485 C mol^{-1};

E^n: the thermoneutral voltage (calculated from ΔH_i^0), V;

E_i: the applied cell voltage, V.

The energy efficiency of total CO_2 electrolysis products reported in this work is the sum of that of each individual product.

The single-pass utilization efficiency, the amount of unreacted CO_2, converted CO_2 and CO_2 loss were calculated as follows:

$$Single\text{-}pass\ utilization\ efficiency = \frac{Converted\ CO_2}{Input\ CO_2} \times 100\%$$

$$Input\ CO_2 = Unreacted\ CO_2 + Converted\ CO_2 + CO_2\ loss$$

Input CO_2 was kept constant at 29.5 or 14.7 mL min^{-1} and could be quantified by on-line GC at open circuit voltage (OCV).

$$Converted\ CO_2 = Produced\ CO = \frac{FE_{CO} \times 60 \times I \times 22.4 \times 1000}{2 \times 96485}\ mL\ min^{-1}$$

Here, I refers to the applied total current, A.

$$CO_2\ loss = Consumed\ CO_2 - Converted\ CO_2$$

Consumed CO_2 was calculated by the difference in CO_2/N_2 GC peak area ratio at open circuit voltage (OCV) and applied current densities.

$$Consumed\ CO_2 = (CO_{2in}/N_{2in} - CO_{2out}/N_{2out})\ /\ (CO_{2in}/N_{2in}) \times\ v_{CO2}\ \ mL\ min^{-1}$$

CO_{2in} and N_{2in} were the GC peak areas of CO_2 and N_2 of the inlet gas at OCV;

CO_{2out} and N_{2out} were the GC peak areas of the outlet gas at applied current densities.

$$Unreacted\ CO_2 = Input\ CO_2 - Converted\ CO_2 - CO_2\ loss$$

Contact angle measurements

Contact angle measurements were conducted by a DSA100 Drop Shape Analyzer.

Video was recorded when water was being pumped to the drop slowly from the syringe

via the needle, and the water front advances on the sample. Each image of this video

was later analyzed to determine the contact angle at the moment the image was captured.

Computational details

Density functional theory (DFT) calculations were performed using Vienna ab initio

simulation packages (VASP).[3] All calculations were performed spin-polarized using

the projector-augmented wave (PAW)[4] pseudopotentials and the Perdew-Burke-

Ernzerhof (PBE)[5] exchange-correlation functional. The plane wave cutoff was set to

400 eV. The convergence of energy and forces were 1×10^{-4} eV and 0.05 eV·Å^{-1},

respectively. A $2 \times 2 \times 1$ Monkhorst-Pack[6] grid and a 6x6x1 grid of k-points was used to

sample the first Brillouin zones of the surfaces for structural optimizations and Bader

charge analysis, respectively. All atoms were fully relaxed during structural

optimizations. The DFT-D3 method was used to consider the dispersion correction

caused by van der Waals interactions.[7] The VASPsol package was used for implicit

solvation corrections.[8]

A periodically repeated single-layer graphene model with the Ni-N_2 single-atom

active-site structure embedded in the in-plane matrix has been built to simulate the Ni-

N-C catalysts with a 5×5 unit cell in size of (12.3 Å × 12.3 Å)sin60° and a vacuum slab height of 17 Å. To simulate the solvent microenvironment around the active site, one explicit layer of water molecules was added onto the catalyst surface.

The free energy was calculated with the vibrational frequency corrections: $G = E_{DFT} + ZPE + \int C_p dT - TS$, where E_{DFT} is the DFT-calculated total energy, ZPE is the zero-point vibrational energy, $\int C_p dT$ is the heat capacity, T is the temperature, and S is the entropy. The correction values used for molecules and adsorbates were consistent with our previous work.[1]
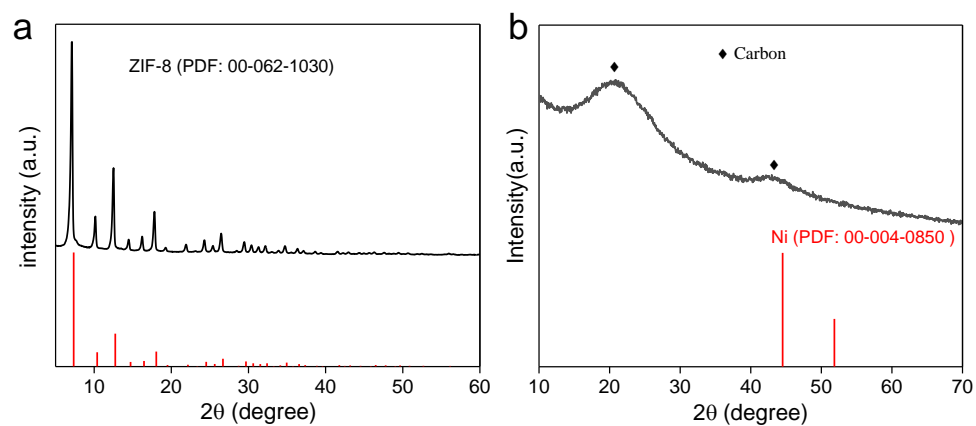
Fig. S1. XRD patterns of Ni-ZIF-8 precursor (a) and Ni-N-C catalyst (b). The X-ray diffraction (XRD) pattern of the Ni-ZIF-8 precursor shows typical diffraction peaks of ZIF-8. The XRD pattern of Ni-N-C catalyst shows typical diffraction patterns of amorphous carbon and no peak assigned to Ni can be observed.[1]
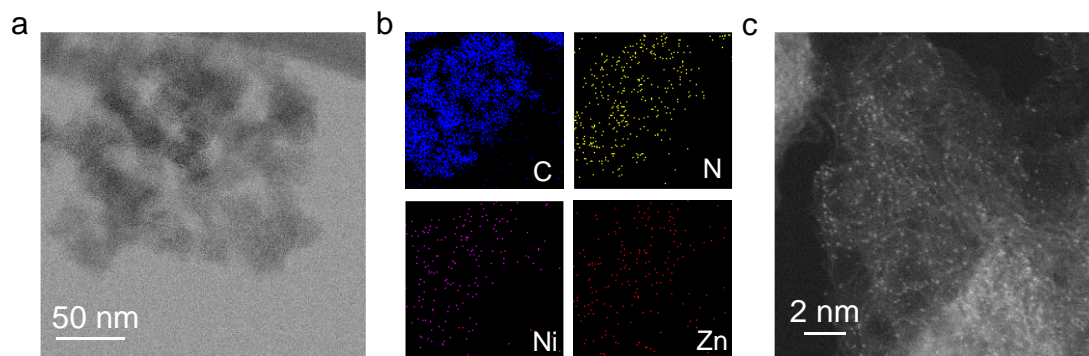
Fig. S2. (a) HRTEM image of Ni-N-C catalyst and (b) the corresponding EDS images for C, N, Ni, and Zn. (c) HAADF-STEM image of Ni-N-C catalyst.
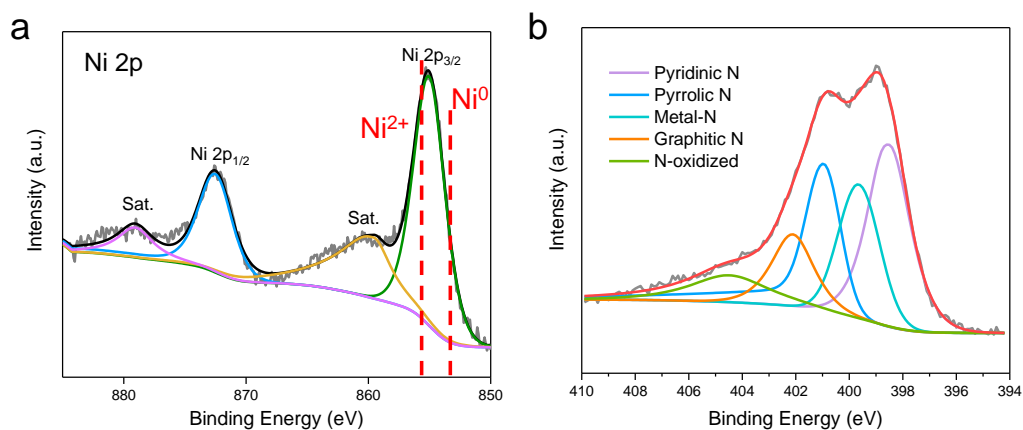
Fig. S3. Ni 2p (a) and N 1s (b) XPS spectra of Ni-N-C catalyst. The binding energy of the Ni 2p3/2 peak in the Ni-N-C catalyst is around 855.0 eV, higher than that of metallic Ni^0 (~853.0 eV) and lower than that of Ni^{2+} (~855.7 eV), indicative of a valence of Ni species between 0 and +2.[1]
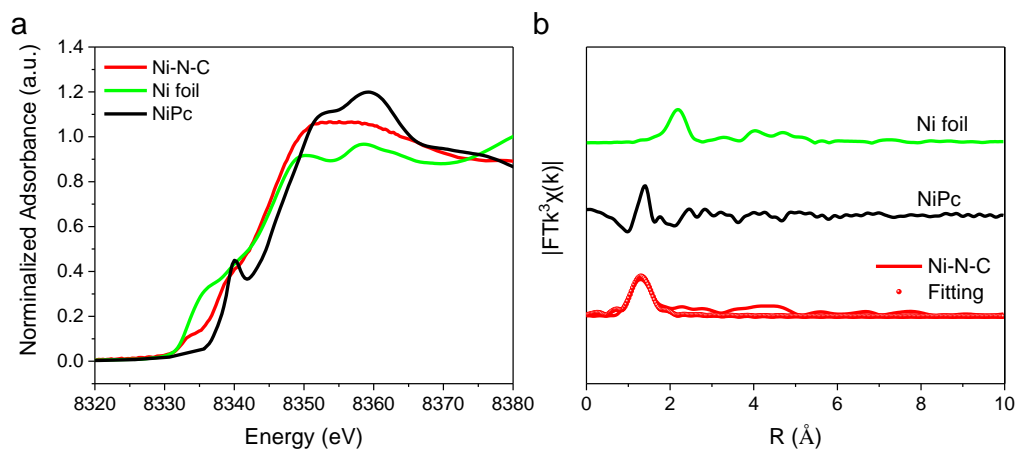
Fig. S4. (a) Ni K edge XANES spectra; (b) Fourier transformed (FT) k^3-weighted $\chi(k)$-function of the EXAFS spectra for Ni K edge.
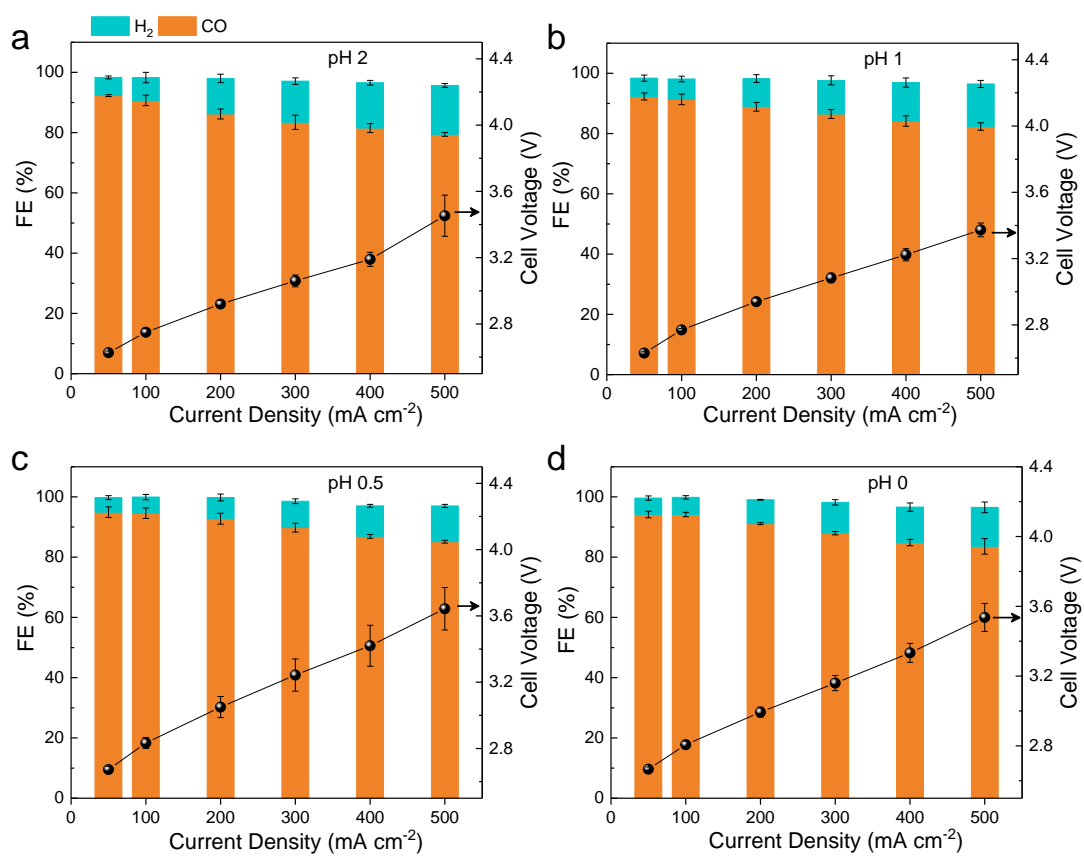
Fig. S5. FEs of CO and H_2 and cell voltage as a function of current densities over Ni-N-C catalyst in 0.5 M K_2SO_4 + H_2SO_4 anolyte with pH 2 (a), 1 (b), 0.5 (c), and 0 (d). The error bars represent standard deviation from three independent measurements.
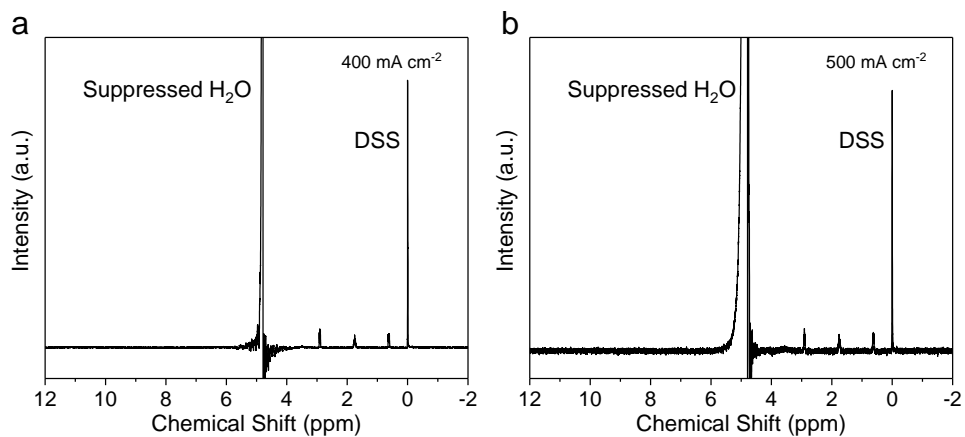
Fig. S6. ^{1}H-NMR spectra of outlet electrolytes at 400 (a) and 500 (b) mA cm^{-2}. No liquid products could be detected. The peak at 4.8 ppm is assigned to suppressed H$_2$O, and the peaks at 0, 0.62, 1.75, and 2.91 ppm are assigned to the DSS internal standard.
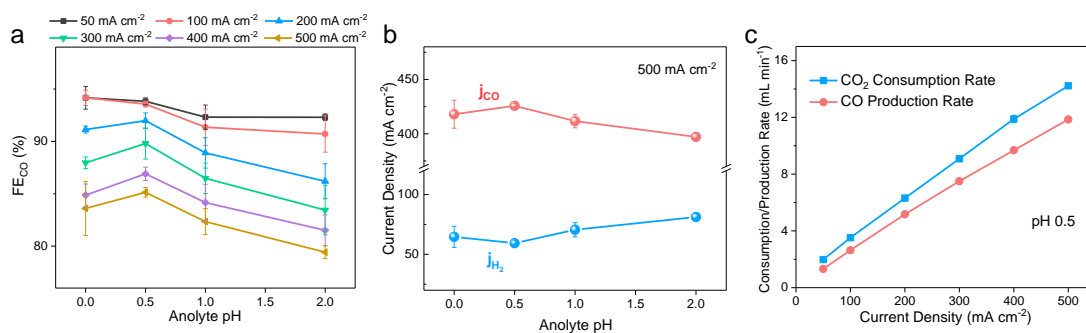
Fig. S7. (a) FE of CO as a function of anolyte pH at 50−500 mA cm^{-2}. (b) Partial current densities of CO and H$_2$ as a function of anolyte pH at 500 mA cm^{-2}. (c) CO$_2$ consumption rate and CO production rate as a function of applied current densities in acidic (0.5 M K$_2$SO$_4$ + H$_2$SO$_4$ anolyte with pH 0.5) MEA electrolyzer. The error bars represent standard deviation from three independent measurements.
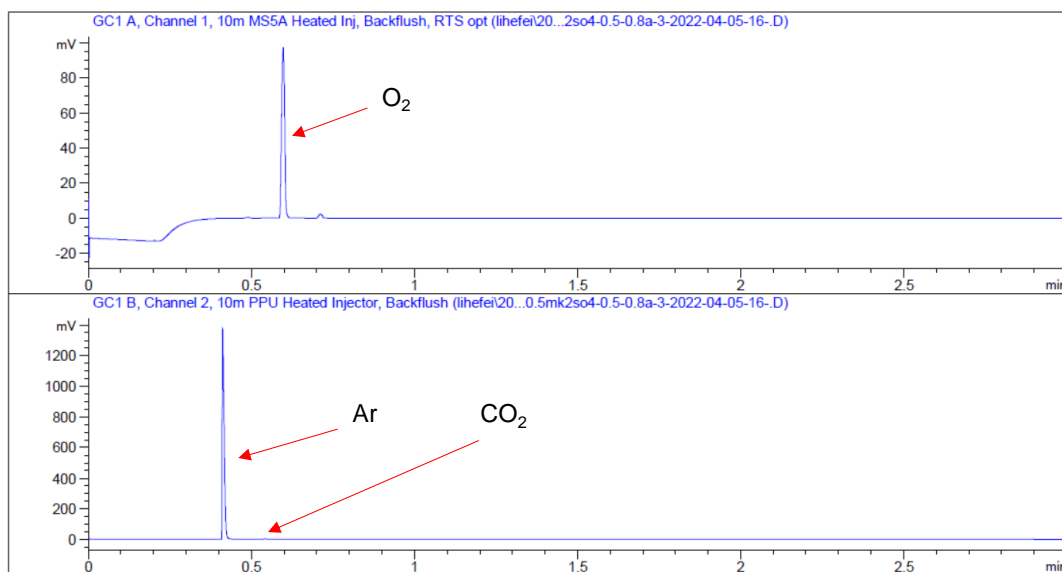
Fig. S8. Gas products in anode detection. A liquid gas mixture was firstly obtained in anode outlet and then separated in a flask. Argon was used as the carrier gas to purge gas products to GC. Trace amounts of CO_2 could be detected except for Ar in Channel 2 of GC.
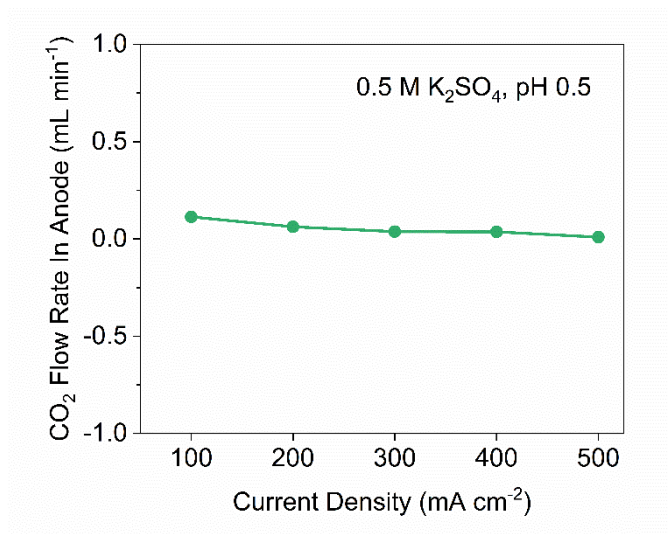
Fig. S9. CO_2 distribution of the outlet gases at the anode side at different current densities in acidic (0.5 M K_2SO_4 + H_2SO_4 anolyte with pH 0.5) MEA electrolyzer. CO_2 flow rate was lower than 0.1 mL min^{-1} at the anode side.
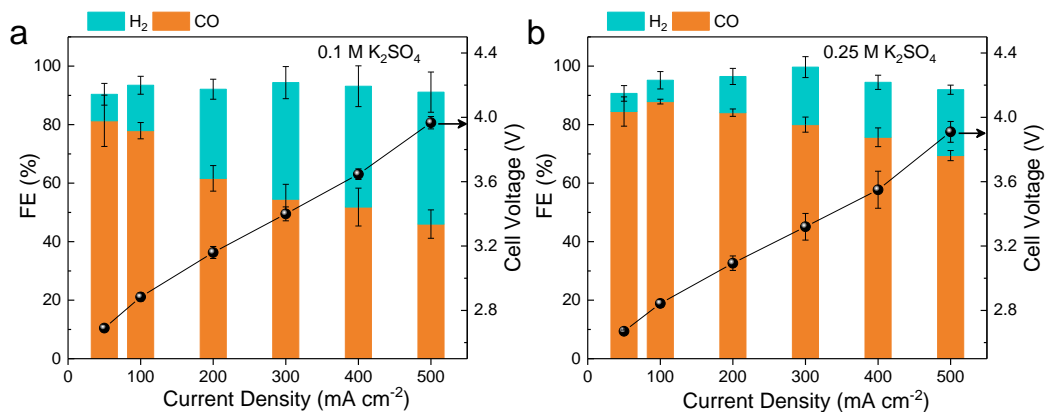
Fig. S10. FEs of CO and H_2 and cell voltage as a function of current densities over Ni-N-C catalyst in acidic (0.1 M (a) and 0.25 M (b) K_2SO_4 + H_2SO_4 anolyte with pH 0.5) MEA electrolyzer. The error bars represent standard deviation from three independent measurements.
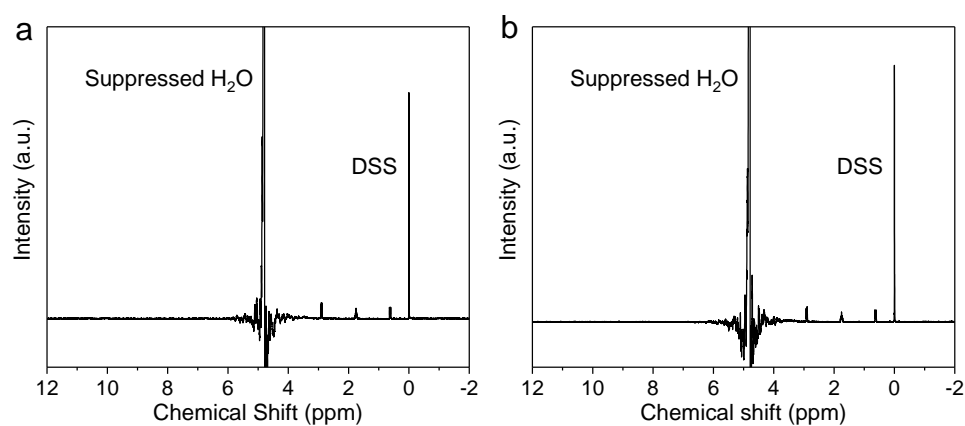
Fig. S11. ^{1}H-NMR spectra of outlet electrolytes at 50 mA cm^{-2} in acidic (0.1 M (a) and 0.25 M (b) K$_2$SO$_4$ + H$_2$SO$_4$ anolyte with pH 0.5) MEA electrolyzer. No liquid products could be detected. The peak at 4.8 ppm is assigned to suppressed H$_2$O, and the peaks at 0, 0.62, 1.75, and 2.91 ppm are assigned to the DSS internal standard.
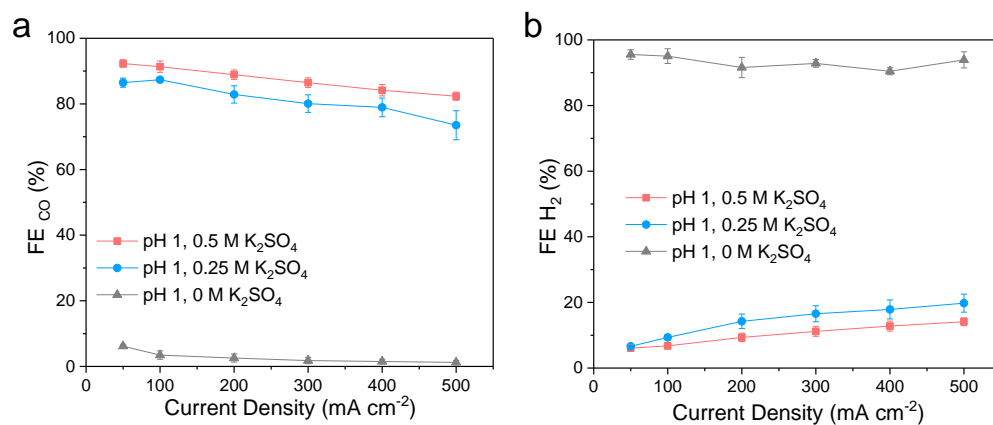
Fig. S12. CO (a) and H_2 (b) FEs as a function of current densities measured in K_2SO_4 + H_2SO_4 anolytes with pH 1 but different K^+ concentrations. The error bars represent standard deviation from three independent measurements.

Fig. S13. (a) FEs of CO and H_2 and cell voltage as a function of current densities measured in 0.5 M K_2SO_4 + H_2SO_4 anolyte with pH 0.5 under 0.5 MPa CO_2. (b) CO production rate as a function of applied current densities measured in 0.5 M K_2SO_4 + H_2SO_4 anolyte with pH 0.5 under 0.1 and 0.5 MPa CO_2. The error bars represent standard deviation from three independent measurements.
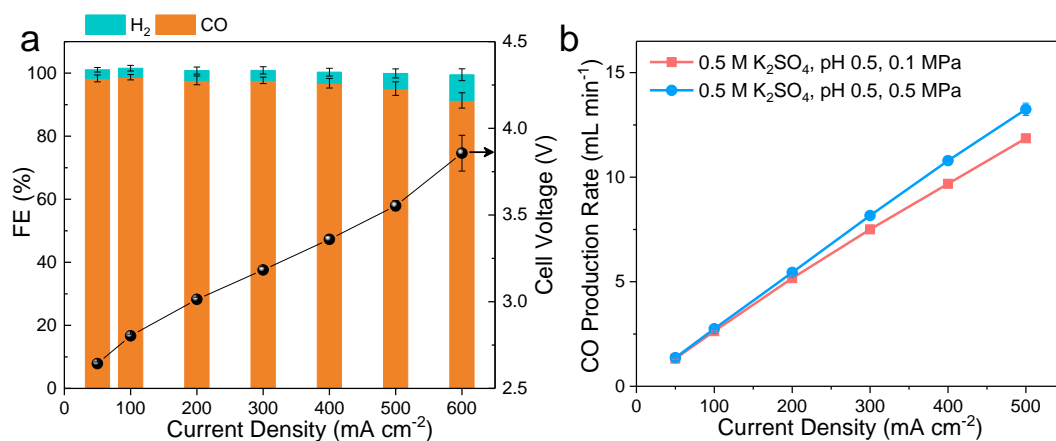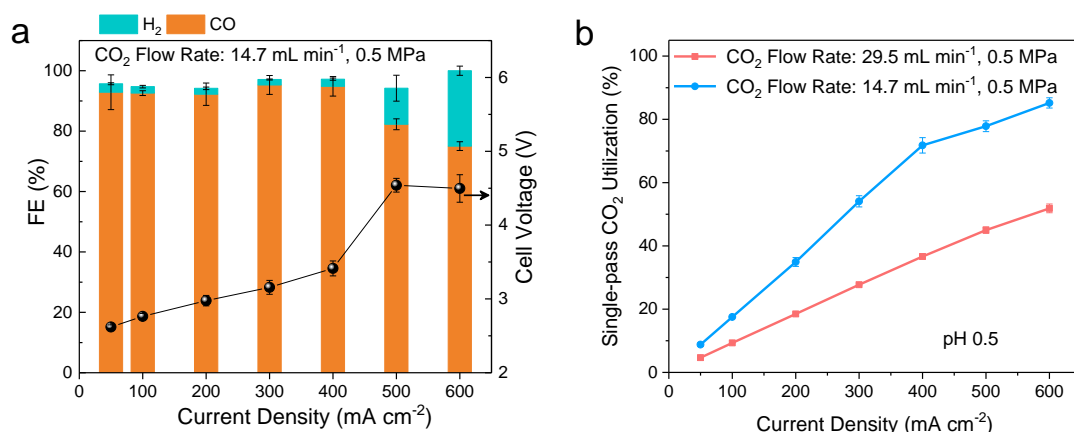
Fig. S14. (a) FEs of CO and H_2 and cell voltage as a function of current densities measured in 0.5 M K_2SO_4 + H_2SO_4 anolyte with pH 0.5 under 0.5 MPa CO_2 at a CO_2 flow rate of 14.7 mL min^{-1}. (b) Single-pass CO_2 utilization efficiency as a function of applied current densities measured in 0.5 M K_2SO_4 + H_2SO_4 anolyte with pH 0.5 under 0.5 MPa CO_2 at different CO_2 flow rates. The error bars represent standard deviation from three independent measurements.
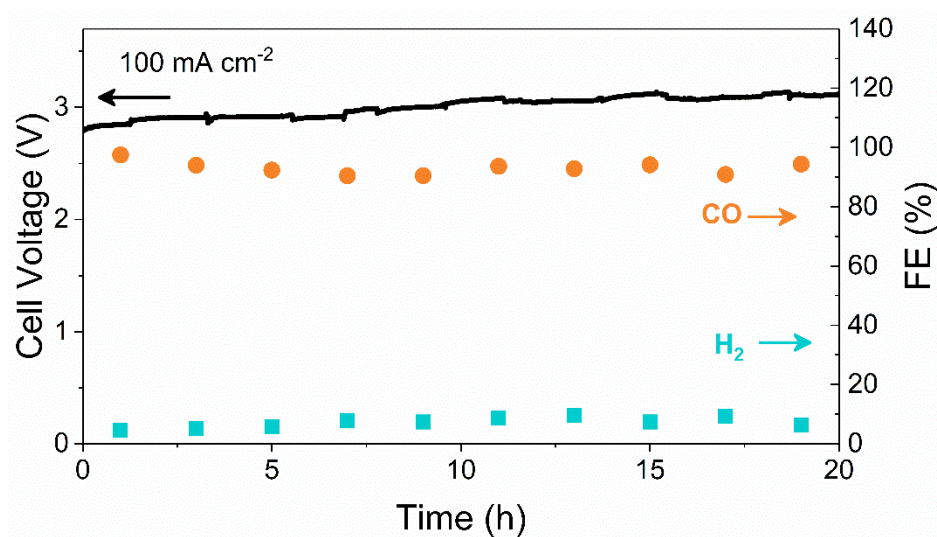
Fig. S15. Stability test of Ni-N-C catalyst at 100 mA cm^{-2} measured in acidic (0.5 M K$_2$SO$_4$ + H$_2$SO$_4$ anolyte with pH 0.5) MEA electrolyzer. The cell voltage slightly increased in a course of 20 h.
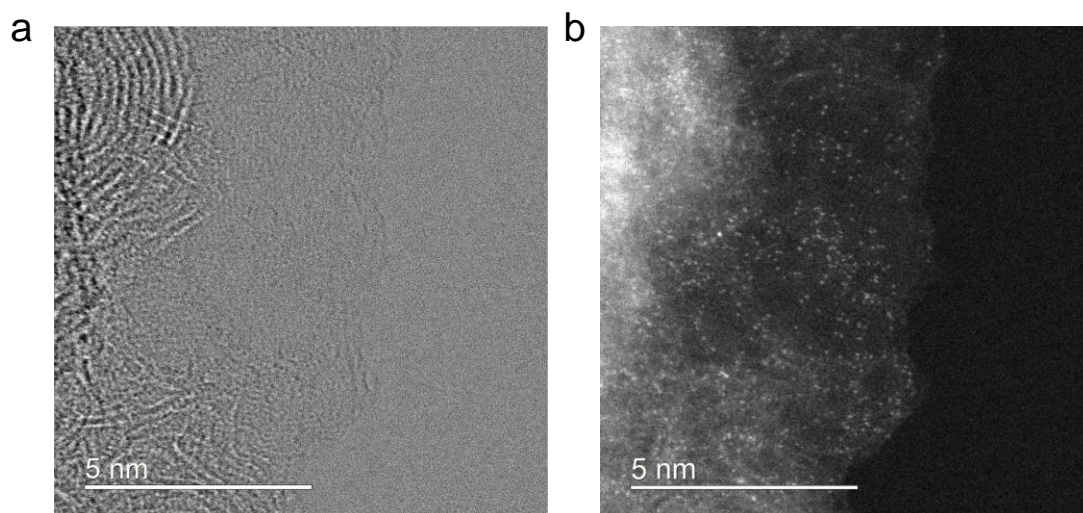
Fig. S16. HRTEM (a) and HAADF-STEM (b) images of Ni-N-C catalyst after stability

test at 500 mA cm^{-2} measured in acidic (0.5 M K$_2$SO$_4$ + H$_2$SO$_4$ anolyte with pH 0.5

under 0.5 MPa CO$_2$) MEA electrolyzer.

a 145.3° b 50.5 °
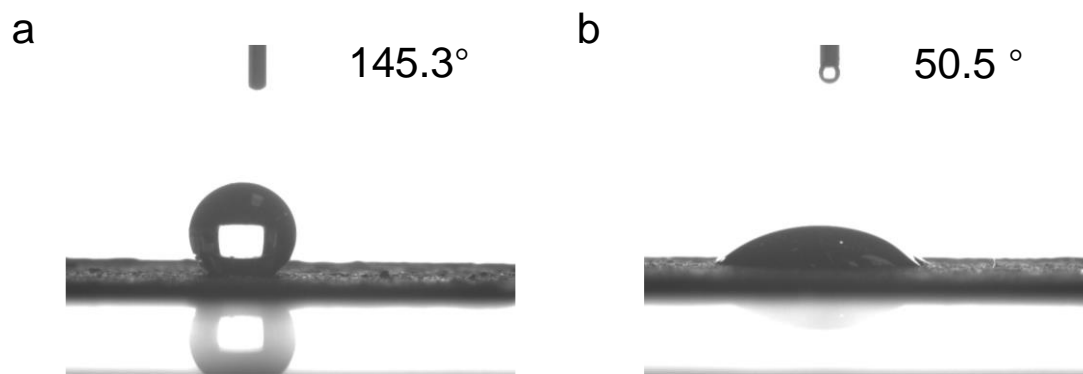
Fig. S17. Contact angle measurements on Ni-N-C electrode before (a) and after (b) 20-hour stability test at 100 mA cm^{-2} in acidic (0.5 M K$_2$SO$_4$ + H$_2$SO$_4$ anolyte with pH 0.5) MEA electrolyzer.
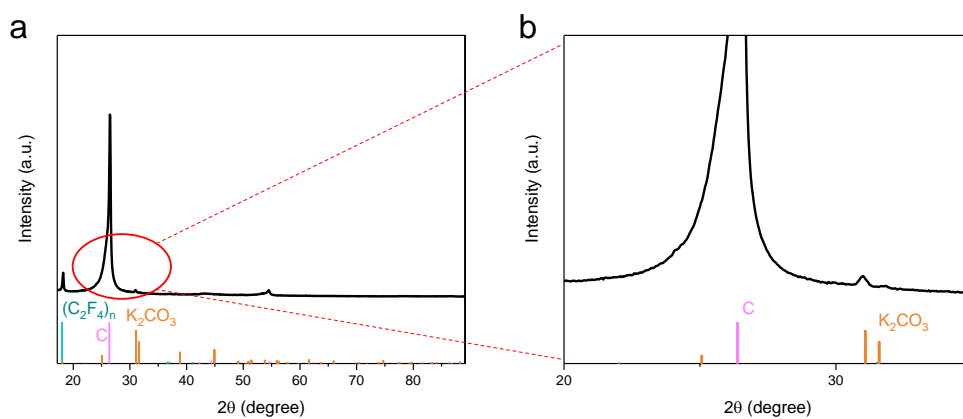
Fig. S18. (a) XRD pattern of Ni-N-C electrode after 8-hour stability test at 500 mA cm^{-2} measured in acidic (0.5 M K_2SO_4 + H_2SO_4 anolyte with pH 0.5 under 0.5 MPa CO_2) MEA electrolyzer. (b) Zoom-in of the XRD patterns in panel (a). A small peak which is assigned to K_2CO_3 appeared (PDF: 01-071-3954).
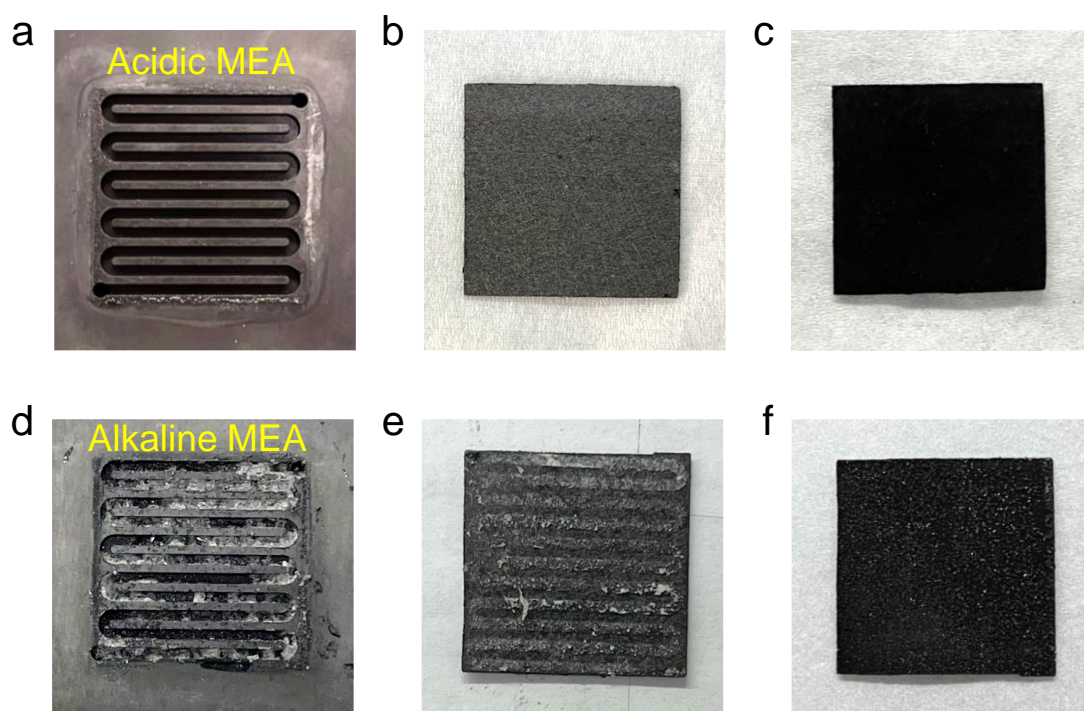
Fig. S19. (a−c) Photos of cathode flow field and Ni-N-C electrode after 8-hour stability test at 500 mA cm^{-2} in acidic (0.5 M K$_2$SO$_4$ + H$_2$SO$_4$ anolyte with pH 0.5 under 0.5 MPa CO$_2$) MEA electrolyzer. (d−f) Photos of cathode flow field and Ni-N-C electrode after 1-hour test measured in alkaline (1 M KOH anolyte) MEA electrolyzer.
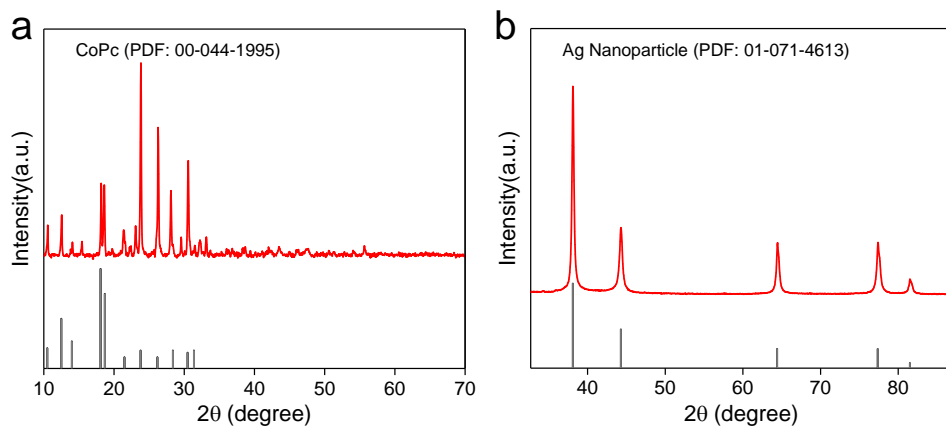
Fig. S20. XRD patterns of commercial CoPc (a) and Ag nanoparticle (b) catalysts.

a

b

1 µm

100 nm
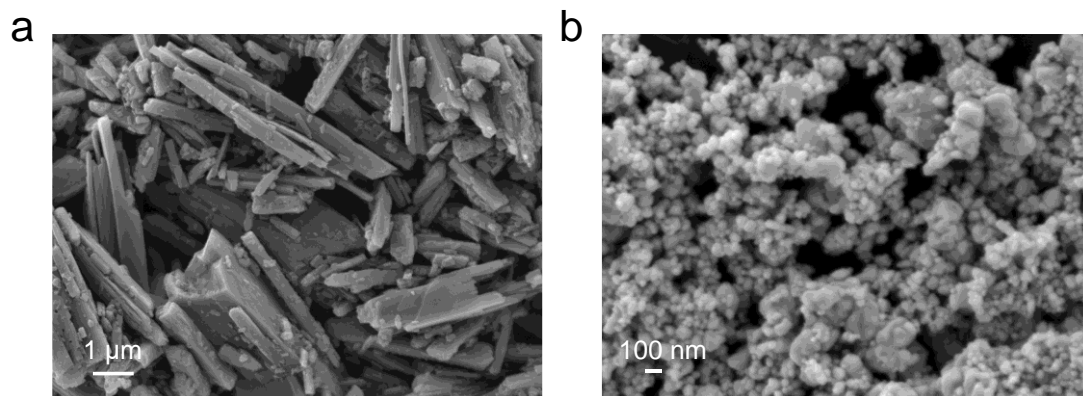
Fig. S21. SEM images of commercial CoPc (a) and Ag nanoparticle (b) catalysts.
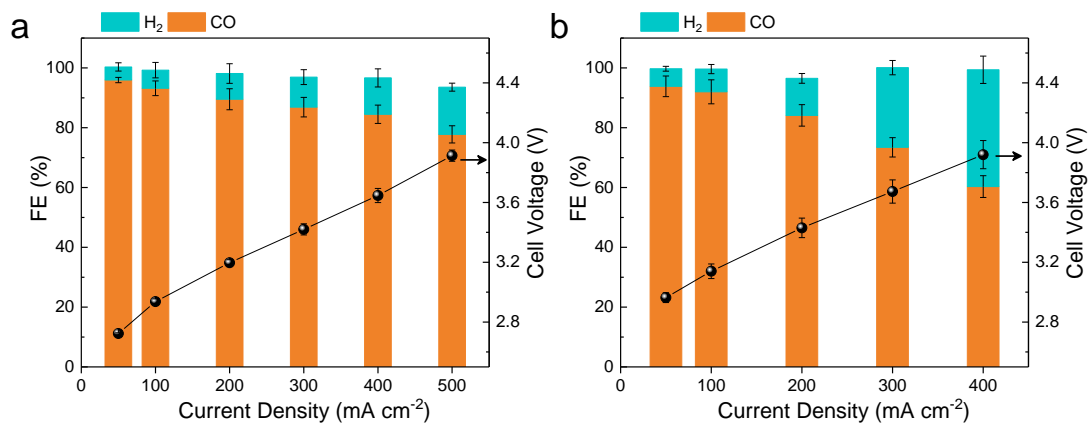
Fig. S22. FEs of CO and H_2 and cell voltage as a function of current densities over CoPc (a) and Ag nanoparticle (b) electrodes measured in 0.5 M K_2SO_4 + H_2SO_4 anolyte with pH 0.5 under 0.5 MPa CO_2. The error bars represent standard deviation from three independent measurements.

H_2O H_3O^+ K^+
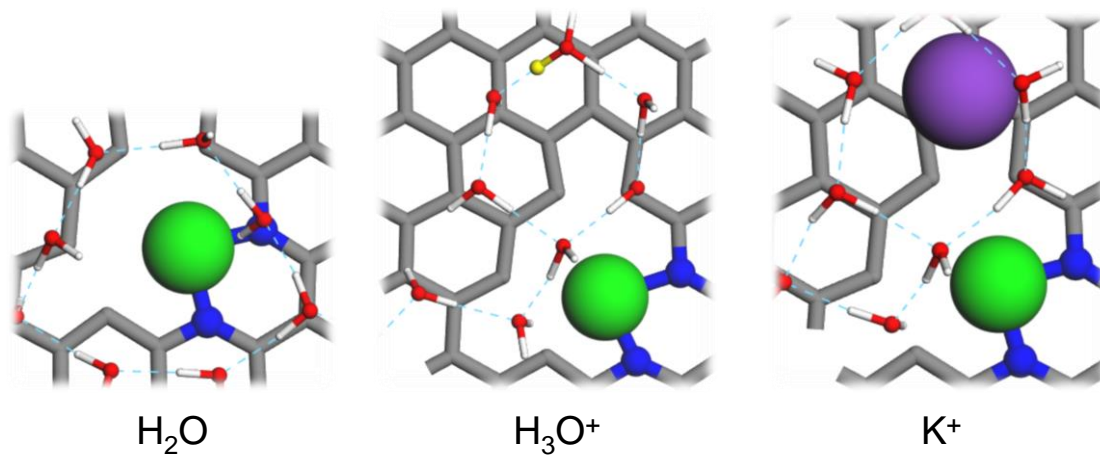
Fig. S23. Top view of atomic scheme of theoretical simulation models in **Fig. 3a**.
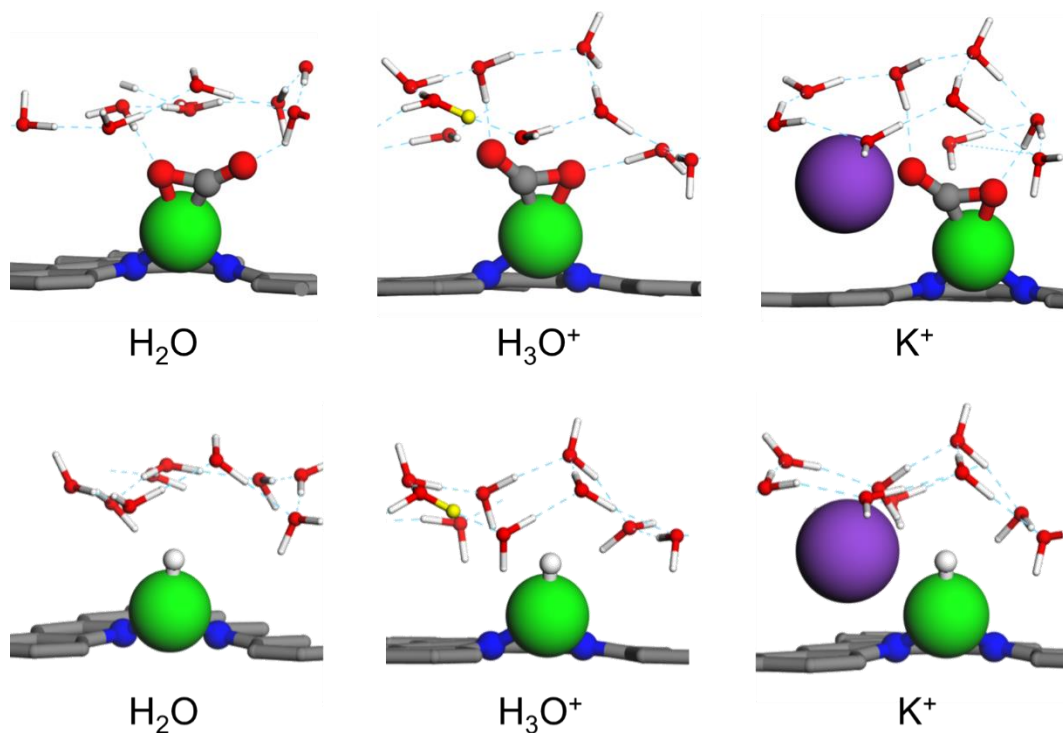
Fig. S24. Atomic scheme of the DFT-optimized adsorption structure of $*CO_2$ (upper panel) and $*H$ (lower panel) at the Ni-N-C catalyst under microenvironment of water solution (H_2O) and with localized hydronium ion (H_3O^+) or potassium ion (K^+). Grey sticks: graphene layer; blue sphere: N; green sphere: Ni, purple sphere: K, red sphere: O, white stick: H, yellow sphere: additional proton in H_3O^+.
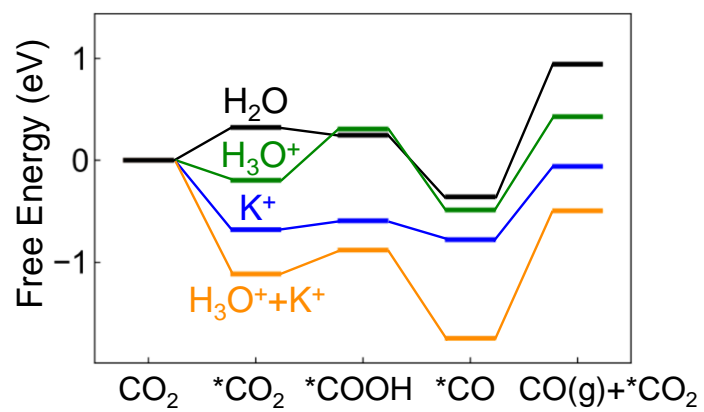
Fig. S25. Free energy diagram for CO_2RR to CO at U = 0 V versus RHE at the Ni-N-C catalyst under local microenvironment of H_2O, H_3O^+, K^+, and $H_3O^+ + K^+$, respectively.
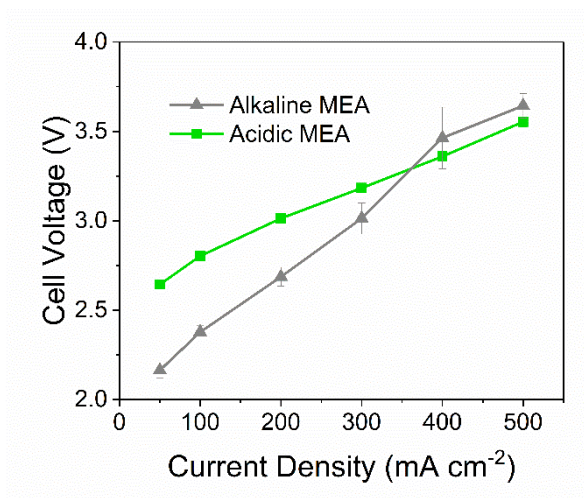
Fig. S26. Cell voltage as a function of applied current density over Ni-N-C catalyst measured in acidic (0.5 M K_2SO_4 + H_2SO_4 anolyte with pH 0.5, 0.5 MPa CO_2) and alkaline (1 M KOH anolyte, 0.5 MPa CO_2) MEA electrolyzers. The error bars represent standard deviation from three independent measurements.
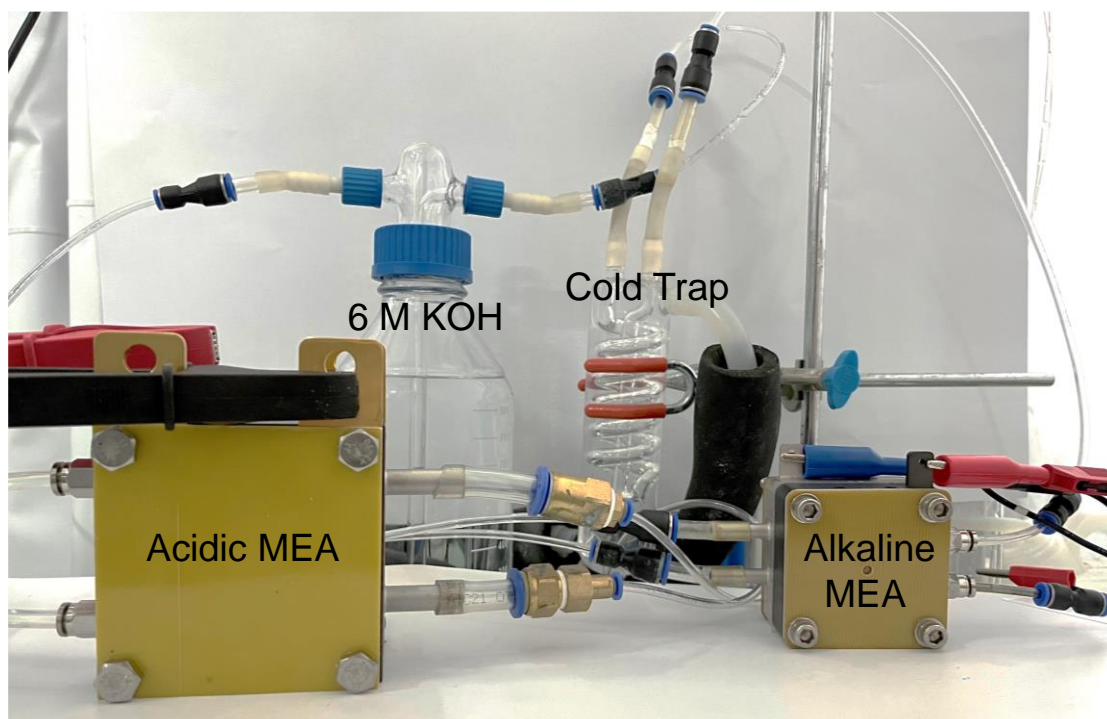
Fig. S27. Photo of two-step CO_2 electrolysis setup consisting of an acidic MEA electrolyzer (25 cm^2) and an alkaline MEA electrolyzer (4 cm^2).

Table S1. EXAFS data fitting results of Ni-N-C for Ni K edge.

Sample	Ni-N CN	R (Å)	D.W.	ΔE_0 (eV)
Ni-N-C	2.1±0.3	1.86	0.0057 (N)	−9.0±1.0

Table S2. H^+ concentration at different pH values and K^+ concentration was kept constant at 1 M.

Anolyte	pH	H^+ concentration (M)	K^+ concentration (M)
$H_2SO_4+K_2SO_4$	0	1	1
$H_2SO_4+K_2SO_4$	0.5	0.31	1
$H_2SO_4+K_2SO_4$	1	0.1	1
$H_2SO_4+K_2SO_4$	2	0.01	1

Table S3. Comparison of acidic CO_2 electrolysis performance over various catalysts.

Catalyst	Anolyte	pH	FE_{CO} (%)	j_{CO} (mA cm^{-2})	Ref.
Ni$_5$@NCN	Na$_2$SO$_4$+H$_2$SO$_4$	1	69.2	26	[9]
Fe-N-C	H$_3$PO$_4$-K$_3$PO$_4$	2	10	1.3	[10]
Ni$_3$N/MCNT	NaCl-HCl	2.5	50.1	-	[11]
Au nanoparticles	Cs$_2$SO$_4$	3	80	160	[12]
Au/C	K$_2$SO$_4$+H$_2$SO$_4$	1.5	91	227	[13]
Ni-N-C/PTFE	Cs$_2$SO$_4$+H$_2$SO$_4$	2	100	250	[14]
Ag powder	Cs$_2$SO$_4$+H$_2$SO$_4$	~0.5	52.5	~105	[15]
Ni-N-C	Cs$_2$SO$_4$+H$_2$SO$_4$	~1	~72	~72	[15]
Ni-N-C	**K$_2$SO$_4$+H$_2$SO$_4$**	**0.5**	**85**	**425 (0.1 MPa)**	**This work**
Ni-N-C	**K$_2$SO$_4$+H$_2$SO$_4$**	**0.5**	**95**	**475 (0.5 MPa)**	**This work**

Table S4. Performance comparison of acidic CO_2 electrolysis in MEA electrolyzers.

Catalyst	Electrolyte	Single-pass CO_2 utilization (%)	CO_2 flow rate (mL min^{-1})	FE_{CO2RR} (%)	j_{total} (mA cm^{-2})	Ref.
Ni-N-C	K_2SO_4+H_2SO_4	77.8	14.7	82	500	This work
Ni-N-C	K_2SO_4+H_2SO_4	85	14.7	75	600	This work
Ni-N-C	K_2SO_4+H_2SO_4	51.8	29.5	91	600	This work
Cu/PCRL	H_2SO_4	~85	1	~53	100	16
Cu/PCRL	H_2SO_4	~16	10	~74	100	16
Ag	Cs_2SO_4+H_2SO_4	~20	10	~70	60	15
Ag	Cs_2SO_4+H_2SO_4	~88	1	~40.5	60	15
Ni_5@NCN	Na_2SO_4+H_2SO_4	~11.8	30	~73	~140	9

Table S5. The amount of dissolved Ni in the outlet electrolyte quantified by ICP-OES.

Reaction condition	Dissolved Ni
100 mA cm^{-2} stability test	Not detected
500 mA cm^{-2} stability test	Not detected

Table S6. A comparison of geometric configuration of simulation results on adsorbed

*CO_2 under the microenvironment of aqueous solution with/without existence of K^+.

d_{M+-O}: distance between the closer O atom in *CO_2 and K^+; $d_{Ni/Au-C}$: distance between

the C atom in *CO_2 and the catalyst surface Ni/Au atom; d_{M+-C}: distance between the

C atom in *CO_2 and K^+; α_{OCO}: bond angle of O-C-O in *CO_2.

	This work (DFT, Ni-N-C)		(AIMD, Au)[17]		(AIMD, Au)[18]	
	H_2O	K^+	H_2O	K^+	H_2O	K^+
d_{M+-O} (Å)	N/A	2.829	N/A	2.86±0.02	N/A	2.5~7.5
$d_{Ni/Au-C}$ (Å)	1.816	1.800	N/A	N/A	~3.5	~4.0
d_{M+-C} (Å)	N/A	3.685	N/A	N/A	N/A	3.0~8.0
α_{OCO} (º)	134.4	133.2	137±5	136±3	~180	~180

Table S7. Raw data on three independent measurements conducted under the same conditions. (pH 0.5, 0.5 M K_2SO_4, 0.1 MPa, 29.5 mL min^{-1})

j_{total} (mA cm^{-2})	Cell Voltage (V)				CO FE (%)				H_2 FE (%)			
	Test 1	Test 2	Test 3	Average±SD	Test 1	Test 2	Test 3	Average±SD	Test 1	Test 2	Test 3	Average±SD
50	2.66	2.66	2.68	2.60±0.01	93.9	93.3	94.1	93.8±0.3	4.9	5.5	4.5	5.0±0.4
100	2.81	2.81	2.84	2.82±0.01	93.4	93.2	93.9	93.5±0.2	5.6	6.2	4.7	5.5±0.5
200	3.01	3	3.18	3.06±0.08	91.8	91.1	92.9	91.7±0.7	7.5	8	6.7	7.4±0.5
300	3.19	3.16	3.38	3.24±0.09	89.1	88.3	91.8	89.7±1.4	9	9.5	7.6	8.7±0.7
400	3.37	3.3	3.59	3.42±0.12	86.1	86.8	87.6	86.9±0.6	10.6	10.2	9.4	10.1±0.4
500	3.59	3.52	3.82	3.64±0.12	84.5	85.3	85.5	85.1±0.4	12.3	11.1	12	11.8±0.5

Table S8. Full data on three independent measurements conducted under the same conditions. (pH 0.5, 0.5 M K_2SO_4, 0.5 MPa, 29.5 mL min^{-1})

j_{total} (mA cm^{-2})	Cell Voltage (V)				CO FE (%)				H_2 FE (%)			
	Test 1	Test 2	Test 3	Average±SD	Test 1	Test 2	Test 3	Average±SD	Test 1	Test 2	Test 3	Average±SD
50	2.65	2.65	2.63	2.64±0.01	99.4	98.6	96.8	98.3±1.0	1.7	3.3	3.1	2.7±0.7
100	2.81	2.81	2.79	2.80±0.01	99.8	98.2	97.9	98.7±0.8	1.5	3.4	3.5	2.8±0.9
200	3.01	3.03	3.00	3.01±0.01	99.3	97.7	95.9	97.7±1.4	1.5	4.1	3.6	3.1±1.1
300	3.17	3.21	3.17	3.18±0.01	99.1	97.0	96.9	97.7±1.0	1.5	4.3	3.5	3.1±1.1
400	3.34	3.39	3.35	3.36±0.02	98.9	95.7	95.6	96.8±1.5	1.9	4.9	3.5	3.5±1.2
500	3.55	3.59	3.52	3.55±0.02	97	92.1	96.1	95.1±2.1	3.4	6.7	4.2	4.8±1.4
600	3.97	3.88	3.72	3.85±0.10	87.9	93.7	92.3	91.3±2.4	10.5	6.0	7.7	8.1±1.8

Table S9. Full data on three independent measurements conducted under the same conditions. (pH 0.5, 0.5 M K_2SO_4, 0.5 MPa, 14.7 mL min^{-1})

j_{total} (mA cm^{-2})	Cell Voltage (V)				CO FE (%)				H_2 FE (%)			
	Test 1	Test 2	Test 3	Average±SD	Test 1	Test 2	Test 3	Average±SD	Test 1	Test 2	Test 3	Average±SD
50	2.66	2.6	2.6	2.62±0.02	92.3	86.1	100.1	92.8±5.7	2.8	2.3	3.2	2.8±0.3
100	2.82	2.73	2.74	2.76±0.04	92.2	91.8	93.6	92.6±0.7	2.2	1.5	2.6	2.1±0.4
200	3.07	2.9	2.96	2.97±0.07	90.8	88.5	97.2	92.2±3.6	2.1	1.3	2.3	1.9±0.4
300	3.29	3.08	3.10	3.15±0.09	91.5	95.1	99.2	95.2±3.1	1.9	1.5	1.9	1.8±0.1
400	3.55	3.31	3.38	3.41±0.10	90.8	94.8	98.8	94.8±3.2	2.2	2	2.8	2.3±0.3
500	4.41	4.59	4.62	4.54±0.09	84.3	79.9	82.5	82.2±1.7	6.1	13.3	16.3	11.9±4.2
600	4.76	4.36	4.37	4.50±0.18	77.0	73.8	74.2	75.0±1.4	22.8	26.4	25.6	24.9±1.5

References

1. C. Yan, H. Li, Y. Ye, H. Wu, F. Cai, R. Si, J. Xiao, S. Miao, S. Xie, F. Yang, Y. Li, G. Wang and X. Bao, *Energy Environ. Sci.* 2018, **11**, 1204−1210.

2. P. Wei, H. Li, L. Lin, D. Gao, X. Zhang, H. Gong, G. Qing, R. Cai, G. Wang and X. Bao, *Sci. China Chem.* 2020, **63**, 1711−1715.

3. G. Kresse and J. Furthmüller, *Phys. Rev. B* 1996, **54**, 11169−11186.

4. P. E. Blöchl, *Phys. Rev. B* 1994, **50**, 17953−17979.

5. J. P. Perdew, K. Burke and M. Ernzerhof, *Phys. Rev. Lett.* 1997, **78**, 1396−1396.

6. H. J. Monkhorst and J. D. Pack, *Phys. Rev. B* 1976, **13**, 5188−5192.

7. S. Grimme, J. Antony, S. Ehrlich and H. Krieg, *J. Chem. Phys.* 2010, **132**, 154104.

8. K. Mathew, R. Sundararaman, K. Letchworth-Weaver, T. A. Arias and R. G. Hennig, *J. Chem. Phys*. 2014, **140**, 084106.

9. Z. Liu, T. Yan, H. Shi, H. Pan, Y. Cheng and P. Kang, *ACS Appl. Mater. Interfaces* 2022, **14**, 7900−7908.

10. A. S. Varela, M. Kroschel, N. D. Leonard, W. Ju, J. Steinberg, A. Bagger, J. Rossmeisl and P. Strasser, *ACS Energy Lett.* 2018, **3**, 812−817.

11. Z. Wang, P. Hou, Y. Wang, X. Xiang and P. Kang, *ACS Sustain. Chem. Eng.* 2019, **7**, 6106−6112.

12. M. C. O. Monteiro, M. F. Philips, K. J. P. Schouten and M. T. M. Koper, *Nat. Commun.* 2021, **12**, 4943.

13. J. Gu, S. Liu, W. Y. Ni, W. H. Ren, S. Haussener and X. L. Hu, *Nat. Catal.* 2022, **5**, 268−276.

14. X. Sheng, W. Ge, H. Jiang and C. Li, *Adv. Mater.* 2022, **34**, e2201295.

15. B. Pan, J. Fan, J. Zhang, Y. Luo, C. Shen, C. Wang, Y. Wang and Y. Li, *ACS Energy Lett.* 2022, **7**, 4224−4231.

16. C. P. O'Brien, R. K. Miao, S. Liu, Y. Xu, G. Lee, A. Robb, J. E. Huang, K. Xie, K. Bertens, C. M. Gabardo, J. P. Edwards, C.-T. Dinh, E. H. Sargent and D. Sinton, *ACS Energy Lett.* 2021, **6**, 2952−2959.

17. M. C. O. Monteiro, F. Dattila, B. Hagedoorn, R. García-Muelas, N. López and M. T. M. Koper, *Nat. Catal.* 2021, **4**, 654−662.

18. D. Le and T. S. Rahman, *Nat. Catal.* 2022, **5**, 977−978.